ELSEVIER

Coastal Engineering 26 (1995) 57–75

COASTAL ENGINEERING

Subgrid modeling of moveable-bed bottom friction in wind wave models [1]

Hendrik L. Tolman

UCAR visiting scientist, Ocean Modeling Branch, Environmental Modeling Center, NOAA/NCEP, 5200 Auth Road, Room 209, Camp Springs, MD 20746, USA

Received 23 December 1994; accepted 22 May 1995

Abstract

A subgrid moveable-bed bottom friction model is developed for use in large-scale wind wave models. This model defines a representative bottom roughness based on the local application of a discontinuous roughness model and a statistical description of depth, sediment and wave parameters for a finite area within the model (i.e., a grid box). The model reproduces the discontinuous attenuation behavior of swell in conditions of initial ripple formation as predicted by a small-scale model. It furthermore suppresses non-physical oscillations of swell energy and unrealistically strong dependencies of depth-limited wave heights on sediment parameters. An alternative interpretation of the model explains the (continuous) transition between the no-ripple and ripple regimes as sometimes observed in nature.

1. Introduction

In the modeling of wind-waves in shallow water, bottom-friction plays an important role (e.g., Shemdin et al., 1978; SWIM Group, 1985). The hydrodynamics of bottom friction for wind waves are fairly well understood (e.g., Weber, 1991). Modeling bottom friction, however, is complicated by interactions between waves and sediment. Wave–sediment interactions manifest as ripple formation and as apparent roughness related to sheet flow of sediment in the wave boundary layer. Ripple formation can have a dramatic effect on the bottom roughness length scale k_N (Nikuradse equivalent sand grain roughness); the roughness can range from skin friction with $k_N = O(10^{-4}\ \mathrm{m})$, to well developed ripples with $k_N = O(10^{-1}\ \mathrm{m})$. This large range of possible roughnesses qualitatively explains the large range of decay scales and friction factors observed for swell (Shemdin et al., 1978). A moveable-bed roughness model has been available for over a decade (Grant and Madsen,

[1] OPC contribution Nr. 102.

0378-3839/95/$09.50 © 1995 Elsevier Science B.V. All rights reserved
SSDI 0378-3839(95)00016-X

1982). Although this model appears to be well established in the sediment transport community, its has been implemented (to the knowledge of the present author) in a wave model only once (Graber and Madsen, 1988).

Recently, Tolman (1994) assessed the potential effects of moveable-bed roughness for wind waves using a modified version of the Grant and Madsen roughness model. By analyzing spatial decay scales of the wave field, Tolman has shown that moveable-bed roughness and initial ripple formation are potentially important for swell propagation in shelf seas away from the shore [that is, where horizontal scales of the bathymetry are O(10 km) or larger]. In such conditions, the roughness is governed by the decay rate of the wave field, as will be illustrated in section 2. Moveable-bed effects are not expected to dominate severely depth-limited wind seas, because such wave conditions usually result in vigorous near-bottom wave motion. Bed forms then are washed out and roughnesses are generally small and exhibit limited variability.

Tolman (1994) advocates a subgrid approach when a moveable-bed roughness model is implemented in a large-scale wave model because (i) the spatial decay scales for swell in conditions of initial ripple formation are generally not resolved by wave models, and because (ii) a single roughness might not be representative for an entire grid box in conditions of initial ripple formation. Note that subgrid modeling is not expected to be relevant for severely depth-limited wind seas, as the corresponding roughness regimes are generally far removed from the discontinuity of the roughness model. However, initial ripple formation does result in large changes of the roughness for mildly depth-limited wind seas, where subgrid modeling might influence model behavior.

The present paper addresses subgrid modeling of moveable-bed bottom friction. The starting point is the hydrodynamic model of Madsen et al. (1988) and a modified version of the roughness model of Grant and Madsen (1982) as used by Tolman (1994) (see section 2). This model is shown to result in quasi-random behavior in space, if the required depth and sediment parameters are described with minimal random variability. In section 3 and in the Appendix a statistical subgrid model is derived. In section 4 this model is applied successfully to an idealized swell case and to an idealized case of depth-limited wave growth. The latter case indicates that a subgrid approach is necessary to avoid nonphysical behavior of a wave model for mildly depth-limited wind seas. In section 5 the application of the present subgrid approach to other moveable-bed roughness parameterizations, and the smooth transition between the no-ripple and ripple regimes as observed by Amos et al. (1988) are discussed.

2. Moveable-bed bottom friction

The (local) bottom-friction source term used in the present study consists of the hydrodynamic model of Madsen et al. (1988) and a modified version of the roughness model of Grant and Madsen (1982) as defined by Tolman (1994).

The hydrodynamic model relates a bottom-friction source term S_b to the corresponding two-dimensional spectrum F. This spectrum can be either the wavenumber spectrum $F(k)$, the wavenumber-direction spectrum $F(k,\theta)$, or the frequency-direction spectrum $F(f,\theta)$.

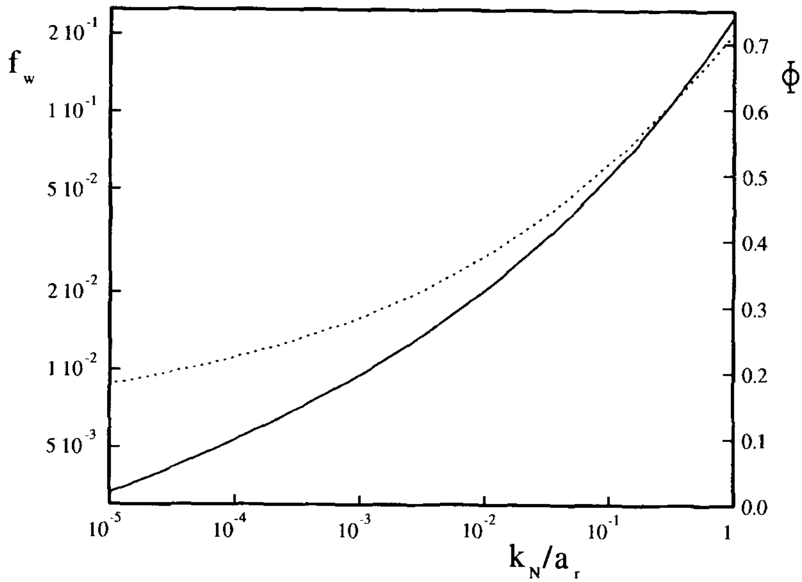

Fig. 1. The friction factor f_w (Eqs. 2 and 3, solid line) and its normalized derivtive Φ (Eq. 17, dotted line) as a function of the relative roughness k_N/a_r.

$$S_b = -f_w u_r \frac{\omega^2}{2g \sinh^2 kd} F \tag{1}$$

$$f_w = \frac{0.08}{Ker^2(2\sqrt{\varsigma_0}) + Kei^2(2\sqrt{\varsigma_0})} \tag{2}$$

$$\varsigma_0 = \frac{1}{21.2\kappa\sqrt{f_w}} \frac{k_N}{a_r} \tag{3}$$

$$u_r = \left(\frac{2\omega^2}{\sinh^2 kd} F\right)^{1/2}, \quad a_r = \left(\frac{2}{\sinh^2 kd} F\right)^{1/2} \tag{4}$$

where $\omega = 2\pi f$ is the radian frequency, d is the depth, f_w is the wave friction factor, k_N is the Nikuradse roughness length, κ is the Von Kàrmàn constant and Ker and Kei are Kelvin functions of the zeroth order. The friction factor f_w (Fig. 1) is a function of the relative roughness k_N/a_r only and f_w is constant for $k_N/a_r > 1$ ($f_w = 0.236$). Finally, u_r and a_r are a representative near-bottom orbital velocity and amplitude, respectively.

Wave–sediment interaction occurs if the near-bottom wave motion is sufficiently strong to move sediment. The ability of the waves to move sediment is governed by the Shields number ψ

$$\psi = \frac{f_w' u_r^2}{2(s-1)gD} \tag{5}$$

where s is the relative density of the sediment compared to water (2.65 for quartz sands), D is a representative grain diameter and the prime in f_w' indicates that the friction factor is

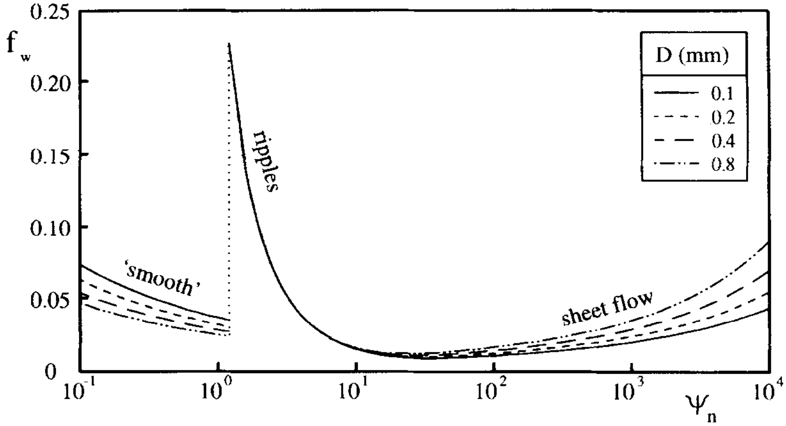

Fig. 2. The friction factor f_w as a function of the normalized Shields number $\psi_n = \psi/\psi_c$ for the moveable-bed roughness model (Eqs. 6, 2 and 3) for various grain diameters D, $\psi_c = 0.05$, $k_{N,0} = 0.01$ m and swell with $f = 0.1$ Hz.

based on skin friction (that is, using $k_N = D$ in Eq. 3). Sediment motion occurs if the Shields number becomes larger than its critical value for initial motion ψ_c (usually determined for monochromatic waves). The critical Shields number ranges from 0.04 to 0.06 for clean, well-sorted sands, to 0.20 or larger for bioturbated or multimodal sands (e.g., Madsen and Grant, 1976; Glenn and Grant, 1987; Drake and Cacchione, 1986; Cacchione et al., 1987; Gross et al., 1992).

If the wave motion is too weak to cause sediment motion (defined here as $\psi/\psi_c < 1.2$), the roughness is set to a pre-defined base roughness $k_{N,0}$, which represents bioturbation, current-induced roughnesses and relict ripples. This roughness is typically of the order of 0.01 m or smaller (Tolman, 1994). If the wave motion is sufficiently strong to generate sediment motion ($\psi/\psi_c \geq 1.2$), the relative roughness k_N/a_r becomes

$$\frac{k_N}{a_r} = 1.5\left(\frac{\psi}{\psi_c}\right)^{-2.5} + 0.0655\left(\frac{u_r^2}{(s-1)ga_r}\right)^{1.4} \tag{6}$$

This equation represents a modified version of the model of Grant and Madsen (1982). The first term on the right represents ripple roughness, and is based on observations of Madsen and Rosengaus (1988) and Madsen et al. (1990). The second term represents sheet-flow roughness, and is based on the model of Wilson (1989). Note that this roughness model differs significantly from the original Grant and Madsen model (see Tolman, 1994, Fig. 2), and that this model is representative for irregular waves and therefore cannot be expected to describe observations for regular waves accurately (see Tolman, 1994, section 3). Furthermore, the model is based on limited laboratory data and requires additional verification. Finally, currents are disregarded in the model, and for simplicity will also be disregarded throughout this paper.

For a given wave frequency f, the relative roughness (Eq. 6) and hence the friction factor becomes a function of the normalized Shields number $\psi_n \equiv \psi/\psi_c$ only (Fig. 2). If no sediment motion occurs ($\psi_n < 1.2$) the bed is relatively smooth with fairly small friction factors [$f_w = O(0.05)$]. In conditions of initial ripple formation ($\psi_n = 1.2$) the roughness discontinuously increases to $k_N/a_r \approx 1$ with $f_w \approx 0.23$ (dotted line). For increasing Shields numbers ripples are washed out, resulting in a decrease of f_w. For $\psi > 10^2$ friction factors increase moderately due to an increasing sheet-flow roughness. Note that both the "smooth bed" roughness $k_{N,0}$ and the sheet flow roughness are independent of the grain diameter D (see Eq. 6). The apparent dependency the friction factor on D for the corresponding flow regimes in Fig. 2 is solely due to the dependency of ψ on D (Eq. 5).

The discontinuous behavior of the roughness model is realistic if the time scale of ripple generation is much smaller than the time scale of evolution of the wave field (as is generally assumed). Even then, the roughness can take any value in the discontinuous range, in particular when the spatial decay scale of the wave field is comparable to the dominant bathymetric scales (Tolman, 1994). This is illustrated below for steady, one-dimensional swell propagation, for which the governing equation is

$$\frac{\partial c_g E}{\partial x} = S_t = -\frac{1}{4g} f_w u_r^3 \qquad (7)$$

where E ($=\iint F$) is the total energy, c_g is the group velocity and S_t is the bottom friction source term integrated over the spectrum (from Eqs. 1 and 4). "Exact" solutions for this equation are calculated using the one-dimensional swell propagation model of Tolman (1994, Appendix), with a spatial resolution of 1 km. In this model, roughnesses within the discontinuous range are calculated from the overall energy balance (Tolman, 1994, Eqs. A2 through A4).

Fig. 3 shows results for a large-scale shoal (chain line in panel a). Sediment and wave conditions are chosen to assure ripple formation on the forward face of the shoal ($D = 0.2$ mm, $\psi_c = 0.05 k_{N,O} = 0.01$ m, $T = 12$ s and, at the input boundary, $H = 4\sqrt{E} = 1.75$ m).

The solid lines in Fig. 3 represent results for a bottom with a "smooth" bathymetry, describing the shoal with minimum variability (but obviously still allowing for ripples in the roughness model). In areas where no ripple formation occurs ($\psi_n < 1.2$ in Fig. 3c), the friction factor is nearly constant and approximately 0.03 (Fig. 3b). Larger friction factors correspond to ripple roughness in conditions of initial ripple formation ($\psi_n = 1.2$ in Fig. 3c). Full ripple formation does not occurs as ψ_n does not exceed 1.2 and as f_w does not reach the maximum value corresponding to full ripple formation ($f_w < 0.23$, see Fig. 2). This implies that the spatial decay scale related to full ripple development is smaller than the dominant bathymetric scale.

The dotted lines in Fig. 3 represent results for a bathymetry and sediment data with random variability added. This variability has a normal distribution, and has no spatial correlation at the grid scale of the "exact" model (1 km). The standard deviation of the grain diameter D and critical Shields number ψ_c are $\sigma_D = \sigma_{\psi,c} = 5\%$, respectively, and the added variability of the depth $\sigma_{d,\mathrm{random}} = 0.25$ m. The corresponding friction factor (Fig. 3b) and Shields number (Fig. 3c) show quasi-random behavior on the scale of the model resolution. The local roughness no longer remains within the discontinuous range of the roughness model as generally $\psi_n \neq 1.2$ (Fig. 3c). The wave height (Fig. 3a) follows the results for the smooth bathymetry (solid line) closely. This was expected, because the spatial decay scale corresponding to ripple formation is similar to the dominant bathymetric scales, and therefore much larger than the spatial scale of the added variability.

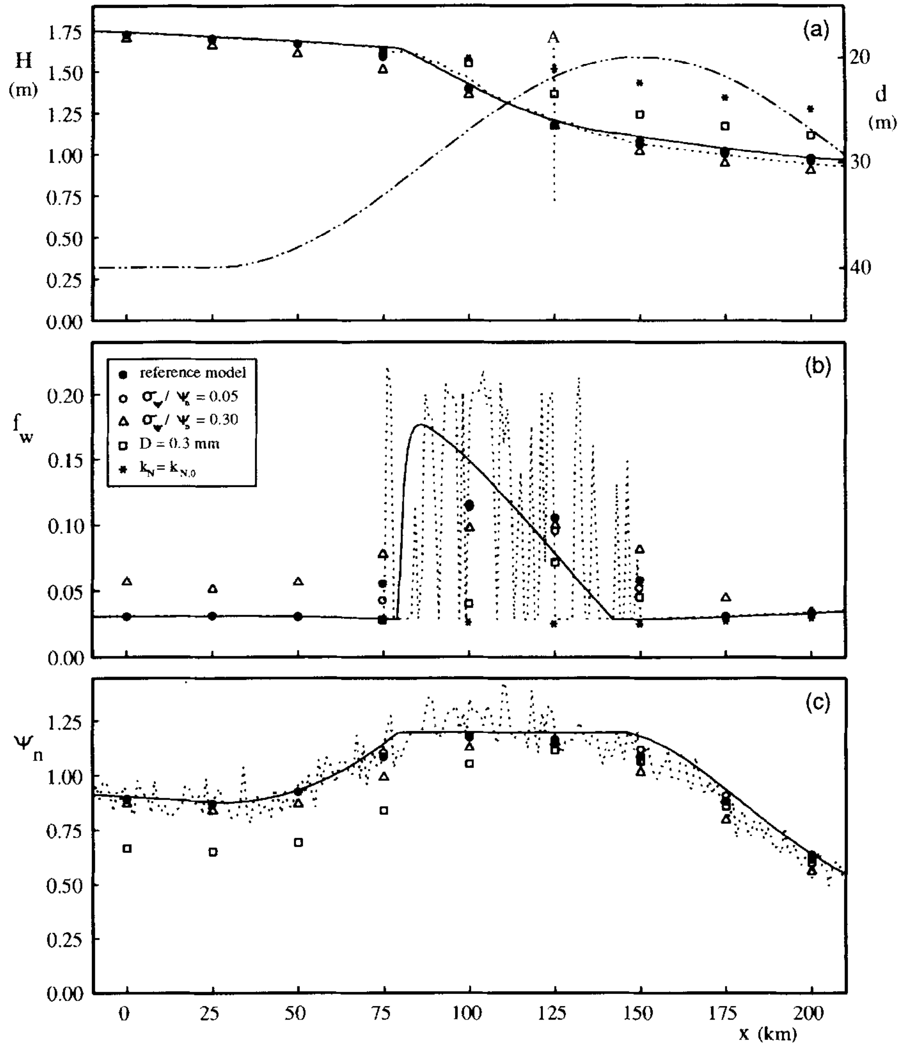

Fig. 3. Wave heights H (a), friction factors f_w (b), and normalized Shields numbers ψ_n (c) for an idealized, one-dimensional swell propagation test. The chain line in (a) represents the bathymetry, $D = 0.2$ mm, $\psi_c = 0.05$, $k_{N,0} = 0.01$ m and $T = 12$ s. Results for the "exact" model ($\Delta x = 1$ km) with a smooth bathymetry and constant sediment parameters (solid lines) and for a bathymetry and sediment with random variability added (dotted lines, $\sigma_D = \sigma_{\psi,c} = 5\%$ and $\sigma_{d,\text{random}} = 0.25$ m). Results for the numerical model ($\Delta x = 25$ km and $\Delta t = 15$ min., symbols) based on the above sediment data and σ_ψ / ψ_n of Eq. (24) with $\sigma_{O,r} = 0.07$ and $(\sigma_{d,g} + \sigma_{d,s})/d$ from the exact model (unless specified differently).

3. A subgrid moveable-bed roughness model

As discussed in the introduction, a moveable-bed roughness model requires a subgrid approach when applied in large-scale numerical wave models. The quasi-random behavior of the friction factor and the Shields number for the irregular bottom (dotted line in Figs.

3b and 3c) suggests the use of a statistical model. Because the roughness model is discontinuous in terms of the normalized Shields number ψ_n, the logical approach is to treat this parameter as a stochastic variable. The statistical properties of ψ_n are determined by the statistical properties of the depth d, the grain diameter D, the critical Shields number ψ_c and the spectrum F (Eqs. 1–6). Due to the integral nature of the Shields number, F can be represented by the significant wave height H and the wave period $T(\equiv f_p^{-1}$, where f_p is the spectral peak frequency). In terms of these mean wave parameters, the representative amplitude and velocity a_r and u_r and the normalized Shields number ψ_n become

$$a_r = \frac{\alpha_a}{2\sqrt{2}} \frac{H}{\sinh k_p d} \tag{8}$$

$$u_r = \frac{\pi \alpha_u}{\sqrt{2}} \frac{H}{T \sinh k_p d} \tag{9}$$

$$\psi_n = \frac{(\pi \alpha_u)^2}{4(s-1)g} \frac{H^2 f_w'}{\psi_c T^2 D \sinh^2 k_p d} \tag{10}$$

where k_p is the wavenumber corresponding to f_p and α_a and α_u are spectral shape factors (Tolman, 1994, Fig. 5). For swell, $\alpha_a = \alpha_u = 1$ and for wind seas both shape factors are somewhat smaller and are slowly varying functions of $k_p d$. To avoid unnecessary complications related to the spectral shape, the dependency of α_a and α_u on $k_p d$ will be disregarded below. The normalized Shields number then is a function of d, D, ψ_c, H and T (Eq. 10; k_p and f_w' follow directly from these parameters). These statistical parameters will be described using their mean value (denoted with suffix m) and their standard deviation σ (e.g., σ_d etc.). For convenience of notation, the vector $\boldsymbol{x} = (d, D, \psi_c, H, T)$ and the corresponding standard deviations σ_1–σ_5 are introduced.

For any function $y(\boldsymbol{x})$, the expected value $\mathrm{E}(y)$ is defined as

$$\mathrm{E}(y) = \int_{\boldsymbol{x}} y(\boldsymbol{x}) p(\boldsymbol{x}) \mathrm{d}\boldsymbol{x} \tag{11}$$

where $p(\boldsymbol{x})$ represents the probability density function (pdf) of $\boldsymbol{x}$. Linearizing Eq. (10) around $\boldsymbol{x}_m$, ignoring possible correlations between components of $\boldsymbol{x}$, the mean normalized Shields number $\psi_{n,m} \equiv \mathrm{E}(\psi_n)$ and its normalized standard deviation $\sigma_\psi / \psi_{n,m} \equiv \sqrt{\mathrm{E}(\psi_n - \psi_{n,m})^2} / \psi_{n,m}$ become

$$\psi_{n,m} = \psi_n(x_m) \tag{12}$$

$$\frac{\sigma_\psi}{\psi_{n,m}} = \left[\sum_{i=1}^{5} \left(X_i \frac{\sigma_i}{x_i} \right)^2 \right]^{1/2} \tag{13}$$

$$X_i = \frac{x_{i,m}}{\psi_{n,m}} \frac{\partial \psi_n}{\partial x_i} \tag{14}$$

where the partial derivatives in (14) are defined at $\boldsymbol{x}_m$. Using the linear dispersion relation $\omega^2 = gk \tanh kd$, $\boldsymbol{X}$ becomes

$$\boldsymbol{X}=\begin{pmatrix} X_d \\ X_D \\ X_{\psi,c} \\ X_H \\ X_T \end{pmatrix}=\begin{pmatrix} \mathscr{F}(2-\Phi') \\ -1+\Phi' \\ -1 \\ 2-\Phi' \\ [2\mathscr{F}(2-\Phi')]-2 \end{pmatrix} \tag{15}$$

where

$$\mathscr{F}=\frac{k_p d}{2n_p \tanh k_p d} \tag{16}$$

$$\Phi=\frac{k_N/a_r}{f_w}\frac{\partial f_w}{\partial(k_N/a_r)} \tag{17}$$

$$n=\frac{k}{\sigma}\frac{\partial\sigma}{\partial k}=\frac{1}{2}+\frac{kd}{\sinh 2kd} \tag{18}$$

The prime in Φ' indicates skin friction ($k_N=D$) as in Eq. (5).

The factors $\boldsymbol{X}$ represent amplification factors between the relative variance of components of $\boldsymbol{x}$ (i.e., $\sigma_i/x_{i,m}$) and the relative spread of the normalized Shields number ($\sigma_\psi/\psi_{n,m}$). Negative values indicate that an increase of x_i corresponds to a decrease of ψ_n.

The factors $\boldsymbol{X}$ are a function of the relative depth $k_p d$ and the normalized derivative of the friction factor for skin friction Φ'. Water depths are generally considered depth-limited for $k_p d<3$. A representative range of Φ' can be estimated from Fig. 1. For sediment motion to occur, a_r is typically O(0.1 m) or larger. With $k_N=D$ O(1 mm) or smaller, k_N/a_r is O(10^{-2})or smaller and Φ' is in the range of 0.2 to 0.4 (see dotted line in Fig. 1).

The behavior of $\boldsymbol{X}$ for the above range of $k_p d$ and Φ' is illustrated in Fig. 4. This figure shows that the dependency of $\boldsymbol{X}$ on Φ' is negligible, both with respect to an intercomparison of components of $\boldsymbol{X}$, and with respect to the dependency of X_d and X_T on the relative depth $k_p d$. For D, ψ_c and H, $\boldsymbol{X}$ is independent of the relative depth. The (absolute) amplifition factors are approximately 0.7, 1 and 1.7, respectively. The amplification factors for the depth d and the wave period T strongly depend on the relative depth $k_p d$. For large relative depths ($k_p d>2$), the relative variability of d and T is strongly amplified ($|X_d|>3$ and $|X_T|>4$). For extremely shallow water, however ($kd>1$), the spread of the Shields number is similar to that of the depth ($|X_d|\approx 1$), whereas it is fairly insensitive to variability of the period T ($|X_T|<0.5$).

The central limit theorem predicts that the pdf of ψ_n can be described using a normal distribution,

$$p(\Psi)=\frac{1}{\sqrt{2\pi}}\,\mathrm{e}^{-0.5\Psi^2},\quad \Psi=\frac{\psi_n-\psi_{n,m}}{\sigma_\psi} \tag{19}$$

for a wide range of pdf's of components of $\boldsymbol{x}$. This is easily confirmed with Monte Carlo experiments (figures not presented here). Given this (or any other) pdf of ψ_n, the representative source term $S_{b,r}\equiv \mathrm{E}(S_b)$ follows from Bayes' theorem as:

$$S_{b,r}=P_I\mathrm{E}(S_b\,|\,\psi_n<1.2)+P_{II}\mathrm{E}(S_b\,|\,\psi_n\geq 1.2) \tag{20}$$

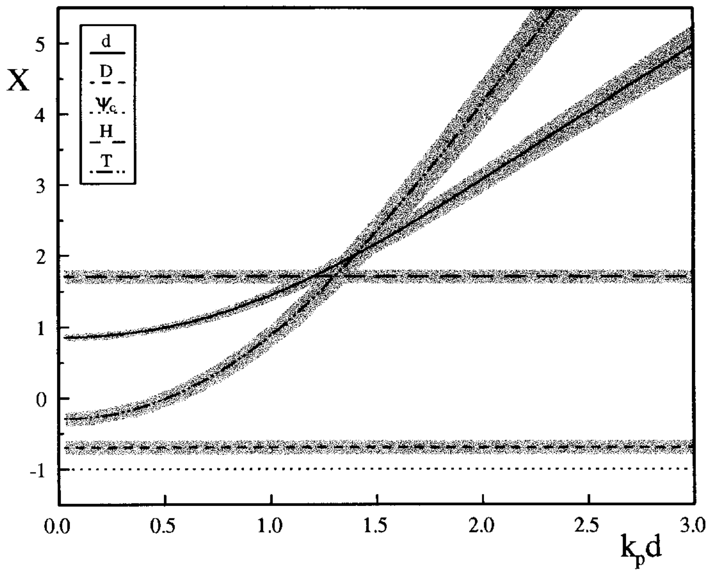

Fig. 4. Amplification factors X of Eqs. (15) as a function of the relative depth k_pd. Lines for $\Phi'=0.3$, shaded areas for Φ' ranging from 0.2 to 0.4.

where $P_I = P(\psi_n < 1.2)$ and $P_{II} = P(\psi_n \leq 1.2)$ represent the probability of occurrence of the no-ripple and ripple regimes, respectively. E(..) represent the corresponding (conditional) expected values of S_b. Note that within this model P_{II} is by definition a fractional ripple coverage for the grid box considered. Explicit approximations for $P_{I,II}$ corresponding to (19) can be found in, for instance, Abramowitz and Stegun (1973, pp. 923–933).

Substituting (1) in (20) and subsequent linearization and elimination of small terms (see Appendix A) results in the following subgrid roughness

$$\frac{k_{N,r}}{a_r} = P_I \frac{k_{IN,0}}{a_r} + P_{II}\left[1.5\psi_{n,II}^{-2.5} + 0.0655\left(\frac{u_r^2}{(s-1)ga_r}\right)^{1.4}\right] \tag{21}$$

$$\psi_{n,II} = \psi_n + p\left(\frac{1.2-\psi_n}{\sigma_\psi}\right)\frac{\sigma_\psi}{P_{II}} \tag{22}$$

The subscripts m are dropped as these equations contain averaged parameter values only (that is, no realizations of stochastic parameters). Substituted in Eqs. (2) and (3), this roughness results in a representative friction factor $f_{w,r}$ and a source term equivalent to Eq. (1).

$$S_{b,r} = f_{w,r} u_r \frac{\omega^2}{2g \sinh^2 kd} F \tag{23}$$

Eqs. (21)–(23), (13)–(19) and (2)–(4) result in a fairly simple subgrid model. The most complicated part of this model is the calculation of the spread of the normalized Shields number (Eqs. 13–18). This part of the model could be simplified further, particularly because the statistical data required to evaluate these equations are generally not available.

The simplest approach possible defines a single universal relative spread of the normalized Shields number. This, however, ignores the potentially strong dependency of σ_ψ/ψ_n on $k_p d$, which is related to the relative spread of the depth and the wave period (Fig. 4). The spread of the depth is generally expected to dominate the spread of the wave period because (i) the differences of the depth between neighbouring grid points around shoals (see, for instance, Fig. 3a) implies a significant subgrid variability of the depth, and (ii) wave periods generally vary slowly in space and time (for swell without currents, the variability of T is generally negligible). The spread of the depth can be divided into two parts. The first is the spread in depth related to the large-scale depth variations resolved by the grid ($\sigma_{d,g}$). This variability can be estimated from the difference in depth between the grid point considered and adjacent grid points. The second component of the spread of the depth d is some universal subgrid spread $\sigma_{d,s}$. Finally combining the relative spread of D, ψ_c and H in a single relative spread $\sigma_{0,r}$, the following simplified expression is found

$$\frac{\sigma_\psi}{\psi_n} \approx \left[\sigma_{0,r}^2 + X_d^2 \left(\frac{\sigma_{d,g} + \sigma_{d,s}}{d} \right)^2 \right]^{1/2} \tag{24}$$

Obviously, X_d can be replace by other (similar) functions of $k_p d$ without loss of generality. The necessity of accurate estimates of σ_ψ/ψ_n will be discussed in the following sections, where several simplified expressions for σ_ψ/ψ_n will be used.

4. Applications

The subgrid moveable-bed roughness model defined by Eqs. (21)–(23), (2)–(4), (19) and estimates for σ_ψ/ψ_n and $P_{I,II}$ is applied to the swell propagation case of Fig. 3 and to an idealized case of depth-limited wave growth. Calculations have been performed with third-generation wave model WAVEWATCH (Tolman, 1991, 1992), in which this source term has been introduced. The appropriate (reduced) equations of WAVEWATCH will be presented below. This model features an integration method for source terms with dynamically adjusted time steps and a second order accurate propagation scheme. To simulate a typical shelf sea model, the grid and time increments are chosen as $\Delta x = 25$ km and $\Delta t = 15$ min. Note that wave models like WAVEWATCH by definition consider the evolution of the wave field in time. Steady solutions have been obtained by continuing the calculation over a sufficiently long time, keeping boundary conditions constant where necessary.

4.1. Swell propagation

The first application of the present model considers the idealized swell propagation case of Fig. 3. In such conditions the governing equation of WAVEWATCH reduces to

$$\frac{\partial F(f,\theta)}{\partial t} + \frac{\partial c_g F(f,\theta)}{\partial x} = S_{b,r}(f,\theta) \tag{25}$$

and swell is simulated by considering energy in a single discrete component of the spectrum only. Excellent results are obtained with the correct sediment data ($D = 0.2$ mm, $\psi_c = 0.05$

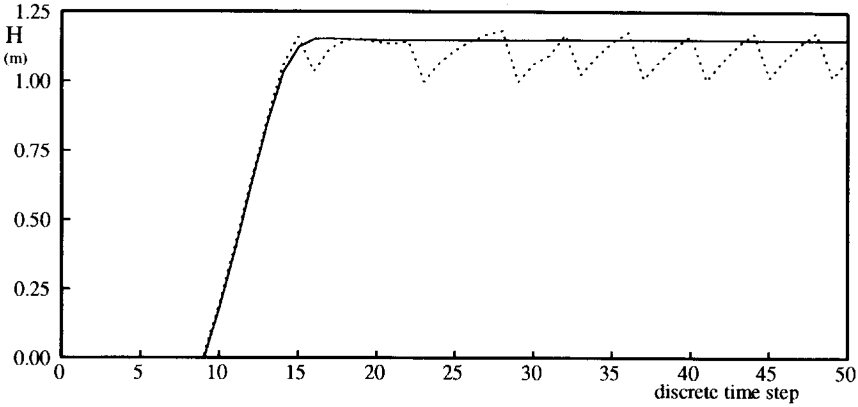

Fig. 5. Evolution in time of the wave height at point A in Fig. 3 for the discontinuous model (dotted line) and the subgrid model (solid line, corresponding to ● in Fig. 3).

and $k_{N,0} = 0.01$ m) and the best possible estimate of σ_ψ / ψ_n based on Eq. (24) (● in Fig. 3). The latter implies that $\sigma_{0,r} = 0.07$ and that $(\sigma_{d,g} + \sigma_{d,s})/d$ is calculated directly from the irregular bottom. The corresponding normalized spread of the Shields number σ_ψ / ψ_n ranges from 0.05 to 0.15. Similarly good results are obtained for a small constant spread $\sigma_\psi / \psi_n \equiv 0.05$ (○ in Fig. 3). Small errors are introduced if the spread is systematically overestimated ($\sigma_\psi / \psi_n \equiv 0.30$, △ in Fig. 3). The friction factor then is systematically overestimated in the no-ripple regime (△ in Fig. 3b) resulting in a slight overestimation of the corresponding decay rate of the wave height (△ in Fig. 3a), and the discontinuous behavior of the attenuation rate is obscured. The model, however, is more sensitive to its mean sediment parameters. If the grain diameter is overestimated by 50% ($D = 0.3$ mm, □ in Fig. 3), the transmitted wave height over and beyond the shoal is significantly overestimated. If ripple formation is neglected altogether ($k_N \equiv k_{N,0}$, $*$ in Fig. 3) errors in the transmitted swell height become even larger.

Note that for the case considered here, a subgrid approach proved necessary to obtain a steady solution. If Eqs. (1)–(6) are used directly, the "steady" solution on the shoal contains systematic modulations of H of up to 20% due to roughnesses alternating between smooth beds and steep ripples (dotted line in Fig. 5).

4.2. Depth-limited wind seas

In this section the subgrid moveable-bed roughness model is applied to depth-limited wave growth, to assess the sensitivity of depth-limited wave heights to sediment conditions, in particular for conditions of initial ripple formation. Depth-limited wave heights are estimated for quasi-homogeneous conditions, for which the governing equation of WAVEWATCH reduces to:

$$\frac{\partial F(f,\theta)}{\partial t} = S_{\rm in}(f,\theta) + S_{\rm nl}(f,\theta) + S_{\rm ds}(f,\theta) + S_{\rm b,r}(f,\theta) \tag{26}$$

The source terms other than $S_{\rm b,r}$ are identical to those of cycle 4 of the WAM model (WAMDIG, 1988; for cycle 4 see, e.g. Mastenbroek et al., 1993). Wind input and dissipation ($S_{\rm in}$ and

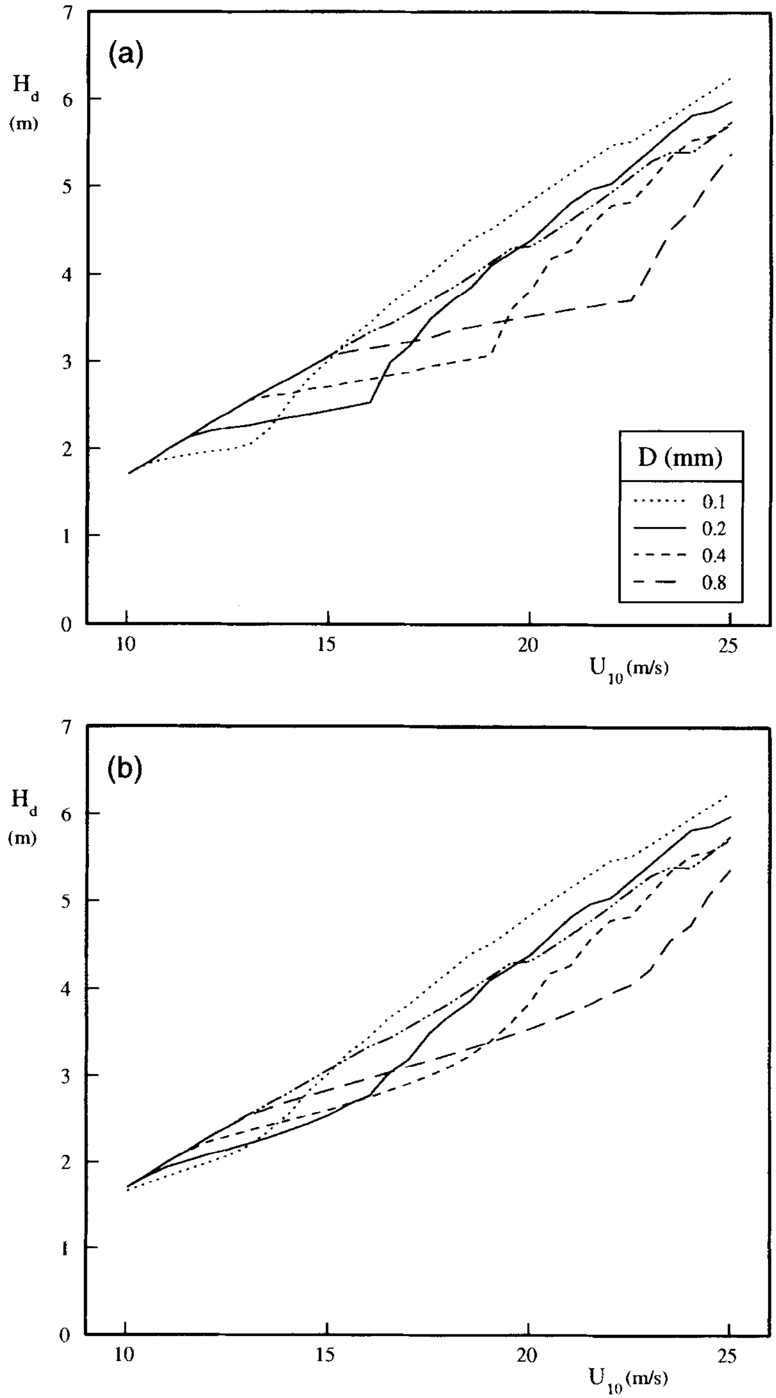
(a)
H_d (m)
0
1
2
3
4
5
6
7
10
15
20
25
U_10 (m/s)
D (mm)
0.1
0.2
0.4
0.8
(b)
H_d (m)
0
1
2
3
4
5
6
7
10
15
20
25
U_10 (m/s)

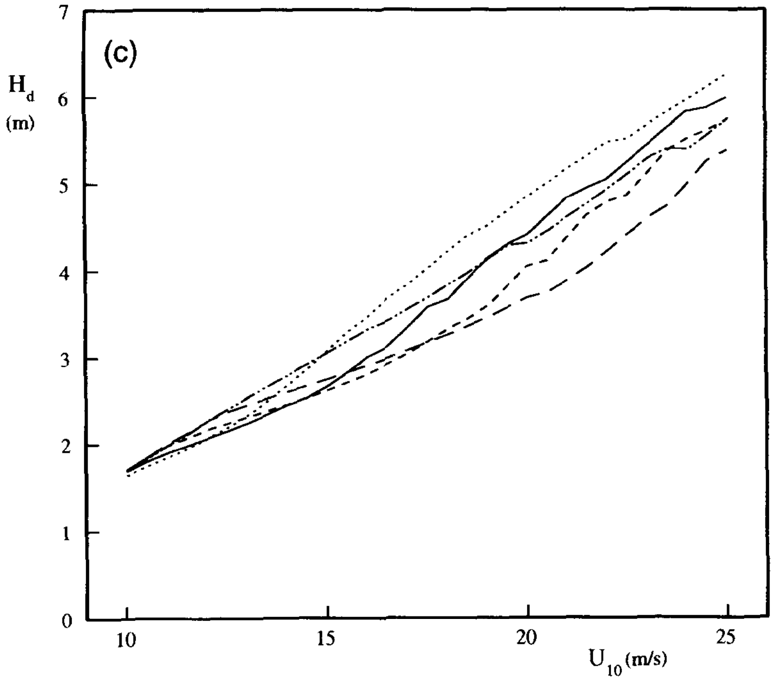
(c)
H_d (m)
0
1
2
3
4
5
6
7
10
15
20
25
U_10 (m/s)

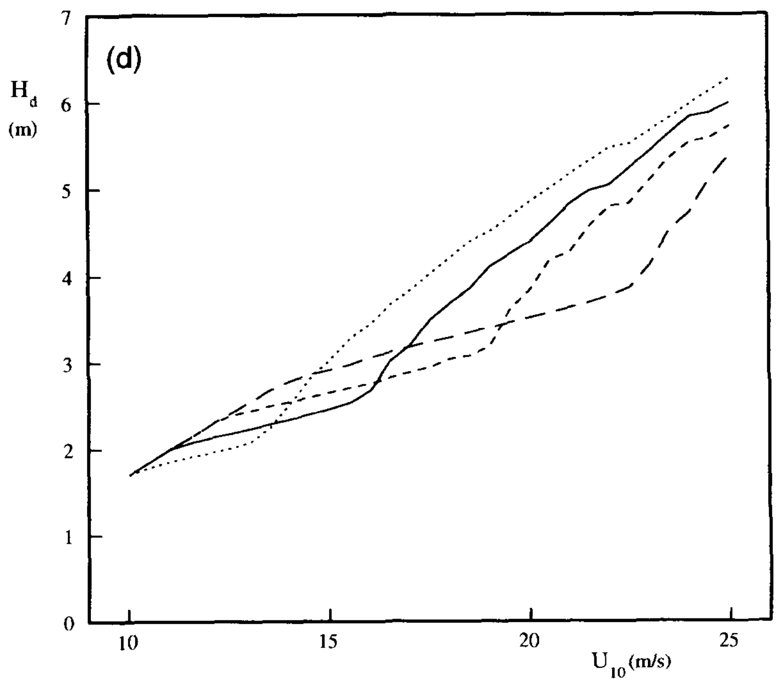
(d)
H_d (m)
0
1
2
3
4
5
6
7
10
15
20
25
U_10 (m/s)

S_{ds}) are modelled according to Janssen (1989, 1991) and nonlinear interactions (S_{nl}) are modelled using the discrete interaction approximation (Hasselmann and Hasselmann, 1985). The spectrum is discretized using 24 directions ($\Delta\theta = 15°$) and 33 frequencies ranging from 0.042 Hz to 0.88 Hz ($\Delta f/f = 0.1$). Due to the dynamically adjusted time step in the integration of the source terms, steady solutions can be found even for the discontinuous roughness model. This will, however, reduce the effective time step by up to an order of magnitude (compared to the continuous subgrid model).

Fig. 6 shows depth-limited wave heights H_d as a function of the wind speed U_{10} for a water depth $d = 20$ m and clean sand with various grain diameters. Presented are results for the discontinuous model of Eqs. (1)–(6) (panel a), and for the present model with ψ_n/σ_ψ estimated from Eq. (24) (panels b and c). The somewhat irregular character of $H_d(U_{10})$ for higher wind speeds is caused by the discrete frequency distribution in the numerical model.

The discontinuous roughness model results in three regimes with distinctly different behavior of $H_d(U_{10})$. For instance for $D = 0.2$ mm, the boundaries of these regimes are at $U_{10} = 12$ m/s and $U_{10} = 16$ m/s (see solid line in Fig. 6a). For the regime with the lowest wind speeds, no sediment motion occurs so that $k_N \equiv k_{N,0}$. The corresponding wave height H_d increases steadily with the wind speed U_{10}. The regime with intermediate wind speeds corresponds to conditions of initial ripple formation where $\psi_n = 1.2$ where the roughness increases sharply with wind speed. The corresponding wave height remains nearly constant. The regime with the highest wind speeds corresponds to near-bottom wave conditions with $\psi_n > 1.2$, including fully developed and partially washed out ripples. At the onset of this regime ripples are washed out rapidly, resulting in a strong increase of H_d with wind speed. Well within this regime, H_d increases steadily, similar to the results of a model with constant roughness k_N (chain line).

The present subgrid model is expected to remove the clear distinction in the behavior of H_d for the separate roughness regimes. This is indeed the case as is illustrated in Fig. 6b and c with results of the present model, estimating the spread of the normalized Shields number using Eq. (24) with $\sigma_{0,r} = (\sigma_{d,g} + \sigma_{d,s})/d = 0.1$ and $\sigma_{0,r} = (\sigma_{d,g} + \sigma_{d,s})/d = 0.2$, respectively. The smaller spreads used (Fig. 6b) are sufficient to remove the large gradients of H_d at the onset of the regime with developed ripples, but leave the different roughness regimes recognizable, in particular for the larger grain diameters. The larger spreads used (Fig. 6c) remove any indication of the existence of a regime with $\psi_n = 1.2$.

Because initial ripple formation typically occurs for $k_p d > 2.5$, the depth dependent part of Eq. (24) has a large effect on the amount of "smoothing" performed by the subgrid model. Even for the relatively small spreads of 10% used in Eq. (24), the total relative spread of the Shields number becomes larger than 40%. If the dependency of σ_ψ/ψ_n on $k_p d$ is neglected, for instance by assuming that $\sigma_\psi/\psi_n \equiv 0.15$, H_d follows the results of the discontinuous model rather closely (Fig. 6d). The relative depth of initial ripple formation

Fig. 6. Depth-limited wave heights H_d as a function of the wind speed U_{10} at a water depth $d = 20$ m for clean sand with various grain diameters (see panel a), $\psi_c = 0.05$ and $k_N = 0.01$ m. (a) Discontinuous moveable-bed roughness model. (b) Present subgrid model with σ_ψ/ψ_n estimated from Eq. (24) with $\sigma_{0,r} = (\sigma_{d,g} + \sigma_{d,s})/d = 0.1$ and (c) $\sigma_{0,r} = (\sigma_{d,g} + \sigma_{d,s})/d = 0.2$. (d) $\sigma_\psi/\psi_n = 0.15$. The chain line represents results for a bottom friction model with constant roughness $k_N = 0.01$ m. Results obtained for wind speed increments of 0.5 m/s.

furthermore decreases with increasing grain diameter D, resulting in a decrease of the corresponding spread of ψ_n and of the amount of "smoothing" of the discontinuous behavior. This explains why the roughness regimes remain the most prominent for larger grain diameters in Fig. 6b.

5. Discussion

A subgrid formulation for a moveable-bed bottom friction source term for application in large-scale numerical wind-wave models is presented. This model combines a subgrid roughness model (Eqs. 21, 22, 19 and corresponding estimates for $P_{I,II}$) with a conventional bottom friction source term (Eqs. 1–4). It furthermore requires an estimate of the relative spread of the Shields number σ_ψ / ψ_n. This spread formally depends on statistical properties of the depth d, the grain diameter D, the critical Shields number θ_c and the wave height and period H and T (Eqs. 13–18). The latter expression for σ_ψ / ψ_n is rather complex, which does not seem to be justified by the simplicity of the remainder of the model, nor by the general lack of data required to evaluate these expressions. A simplified expression is therefore presented in Eq. (24). This expression utilizes information on the variability of the depth from the discrete grid and retains a dependency of σ_ψ / ψ_n on $k_p d$. The latter dependency results in systematically different behavior of σ_ψ / ψ_n for swell and wind seas, which appears important for realistic model behavior in both cases (see below). Consequently, Eq. (24) should not be simplified further.

The present subgrid moveable-bed model shows an excellent description of localized energy dissipation in the idealized swell case of Fig. 3. The discontinuous attenuation behavior shown here is related to initial ripple formation, and can obviously be described by a moveable-bed model only. A moveable bed model in turn requires a subgrid approach, as the decay scales involved are smaller than the grid scale of typical numerical models. The present subgrid model removes nonphysical oscillations from the numerical model, and avoids the need for special treatment of the discontinuous range of the roughness model (as in the model of Tolman, 1994, his Appendix). Swell decay is shown to be sensitive to sediment parameters (Fig. 3), because the discontinuous attenuation behavior is related to initial sediment movement. The model furthermore requires (realistically) small spreads of the Shields number in order to reproduce discontinuous attenuation behavior.

For severely depth-limited wind seas, moveable-bed effects were not expected to be important, as discussed in the introduction. If, however, the moveable-bed model is implemented in a wave model without accounting for subgrid variability, distinct roughness regimes can be observed in the depth-limited wave height for wind seas $H_d(U_{10})$ (Fig. 6a). The occurrence of these distinct regimes is related to the assumption that the bottom roughness behaves identically (and discontinuous) throughout an entire grid box of the numerical model. Considering the quasi-random behavior of the moveable-bed roughness model on subgrid scales in Fig. 3, this assumption does not appear to be realistic. The subgrid model accounts for such variability and is therefore expected to give a better representation of the physics. This model shows less distinct roughness regimes, in particular for smaller grain diameters (Fig. 6b, c). The corresponding depth-limited wave heights H_d are fairly independent of the grain diameter, and behave similar to those of a constant roughness model. This has two implications. First, it is confirmed that moveable-bed effects are generally not important for the modeling of depth-limited wind seas. Secondly, a subgrid approach is needed to avoid unrealistic sensitivities of depth-limited wind seas to sediment parameters if a moveable-bed model is implemented (for instance to accurately describe swell attenuation). The large spread of the normalized Shields number as occurs for large relative depths are essential to remove the above unrealistic behavior.

The present subgrid model has two potential shortcomings. First, the discontinuous roughness model (6) on which the subgrid model is based is not yet satisfactorily validated and is open for improvements (see Tolman, 1994). Secondly, the local applicability of the discontinuous model can be questioned.

The discontinuous roughness model (6) is based on limited laboratory data, and does not include any data in which a mean current is present. Although from a hydrodynamic point of view wave–current interactions are not expected to influence the bottom friction source term significantly (see Tolman, 1994, page 1006), currents can be expected to modify bed forms, and hence influence the roughnesses. In particular in near-shore areas, were currents can be strong, the applicability of the present model therefore is potentially limited. In general, more data is necessary to validate this and other roughness model. In particular field observations and observations including waves and currents would be useful.

The best documented part of the roughness model (6) is its discontinuous behavior as a function of the Shields number (Tolman, 1994). This discontinuous behavior in turn results in the need for a subgrid approach. New parameterizations of moveable-bed roughnesses in different wave–sediment interaction regimes can easily be implemented in Eq. (21). Thus, additional observations might significantly change behavior of moveable-bed roughness models, but are not expected to have an impact on the present subgrid approach, as long as the roughness parameterizations can be expressed in terms of a Shields number.

The present subgrid model assumes the local applicability of the roughness model Eq. (6). This results in extreme changes of the roughness on small scales (Fig. 3b), suggesting the present statistical approach. Such behavior is in qualitative agreement with the observation of small ripple patches in nature (e.g., Cacchione and Drake, 1982), but it is not in agreement with the observations of a transition regime of undeveloped ripples for near-critical Shields numbers as reported by Amos et al. (1988). Amos et al. attribute this transition to a balance between ripple formation by waves and ripple degradation due to bioturbation. This suggests a different approach to modeling a continuous transition between the ripple and no-ripple regimes, using a local ripple evolution model instead of spatial statistics.

A ripple evolution model requires parameterizations for ripple evolution in time. To the knowledge of the present author, data required for such parameterizations is insufficient and qualitative at best (e.g., Brebner, 1980; Amos et al., 1988; Drake and Cacchione, 1989; Green et al., 1990). Such a model could furthermore include statistical information of the local wave field, to estimate the fraction of individual waves which move sediment and hence contribute to ripple formation. Without derivation of an actual model, it appears evident that such a model could be expressed in a form similar to Eq. (21), where P_{II} represents fractional ripple development instead of a fractional ripple coverage (as in the present model). From a wave modeling perspective both approaches are identical, as long as they result in the same representative roughness.

Finally, an alternative interpretation of P_{II} as a fractional ripple development can be used to qualitatively explain the range of Shields numbers for which Amos et al. (1988) observed undeveloped ripples. Assuming (arbitrarily) that undeveloped ripples correspond to $0.05 < P_{\mathrm{II}} < 0.95$ and assuming a normal distribution for ψ_{n} within the spectrum, the transition regime encompasses a range of mean Shields numbers $\Delta \psi_{\mathrm{n}} = 3.3\sigma_{\psi}$. For $\sigma_{\psi}/\psi_{\mathrm{n}} = 0.2$, this results in the ratio of 2 between the highest and lowest Shields number of the transition zone as observed by Amos et al. (1988).

6. Conclusions

A statistical subgrid moveable-bed bottom friction model is developed for the application in large-scale wind wave models. This model accounts for the spatial variability of bottom roughness on subgrid scales. It reproduces the discontinuous attenuation behavior of swell in conditions of initial ripple formation, as predicted by the "exact" model. Application to depth-limited wind seas indicates that a subgrid model is required to avoid an unrealistically strong dependency of mildly depth-limited wind seas on sediment conditions and roughness regimes. The present subgrid approach is easily applied to other (discontinuous) moveable-bed roughness models. An alternative interpretation of the subgrid model can explain the transition regime with undeveloped ripples as observed by Amos et al. (1988).

Acknowledgements

The author thanks Peter Janssen for supplying computer code of his source terms to facilitate implementation in WAVEWATCH, and Dean G. Duffy, Dmitry Chalikov, W. Perrie, Paul E. Long Jr. and D.B. Rao for discussing drafts of this paper.

Appendix A. Derivation of the subgrid model

Substitution of the discontinuous source term (1) in the general subgrid source term (20) yields

$$S_{\mathrm{b,r}} = -\frac{1}{2g}\sum_{\beta} P_{\beta} f_{\mathrm{w},\beta}\, u_{\mathrm{r},\beta} \frac{\omega^2}{\sinh^2 kd} F \tag{A1}$$

where $\beta = \mathrm{I}, \mathrm{II}$ denotes the two ripple regimes as in Eqs. (20) and (21). Assuming that the subgrid model remains quasi-linear with respect to the near-bottom velocity spectrum, this equation becomes

$$S_{\mathrm{b,r}} = -\frac{\omega^2}{2g \sinh^2 kd} F \sum_{\beta} P_{\beta} f_{\mathrm{w},\beta}\, u_{\mathrm{r},\beta} \tag{A2}$$

This equation requires estimates of mean parameter values in both roughness regimes. For an arbitrary parameter $y(\boldsymbol{x})$, linearization gives the following estimate of y_{β}.

$$y_{\beta}=y_{\rm m}+\frac{{\rm Cov}(y,\psi_{\rm n})}{\sigma_{\psi}^{2}}\,(\psi_{{\rm n},\beta}-\psi_{\rm n,m}) \tag{A3}$$

$$\frac{{\rm Cov}(y,\psi_{\rm n})}{y_{\rm m}\psi_{\rm n,m}}=\sum_{i=1}^{5}X_iY_i\left(\frac{\sigma_i}{x_{i,\rm m}}\right)^2 \tag{A4}$$

$$Y_i=\frac{x_{i,\rm m}}{y_{\rm m}}\frac{\partial y}{\partial x_i} \tag{A5}$$

The mean normalized Shields numbers for both roughness regimes are calculated as (using Abramowitz and Stegun, 1973, section 26.2.45)

$$\psi_{{\rm n},\beta}=\psi_{\rm n,m}\mp p\left(\frac{1.2-\psi_{\rm n}}{\sigma_{\psi}}\right)\frac{\sigma_{\psi}}{P_{\beta}} \tag{A6}$$

where the minus is used in the no-ripple regime (β=I) and where $p(...)$ is the standard normal pdf (19). However, the corrections $y_{\beta}-y_{\rm m}$ for $u_{\rm r}$ and $a_{\rm r}$ as given by Eq. (A3) are generally small and their effects partially cancel. Thus Eq. (A2) can be approximated as

$$S_{\rm b,r}=-u_{\rm r,m}\frac{\omega^2}{2g\sinh^2 kd}F\sum_{\beta}P_{\beta}f_{{\rm w},\beta} \tag{A7}$$

Numerical experiments furthermore show that the representative friction factor $\Sigma_{\beta}P_{\beta}f_{{\rm w},\beta}$ can be replaced by a single representative friction factor $f_{\rm w,r}$ calculated from the representative roughness given by Eqs. (21) and (22). Note that Eq. (22) still incorporates an estimate of $\psi_{\rm n}$ specific for the ripple regime. The correction of the normalized Shields number for the ripple regime (right term in Eq. 22) has been maintained to ensure that the corresponding part of the representative roughness remains within its range of validity. Replacing $\psi_{n,\rm II}$ by $\psi_{\rm n,m}$ has a much bigger, impact than the above simplifications, and can lead to differences of O(10%) in the source term.

References

Abramowitz, M. and Stegun, I.A., 1973. Handbook of Mathematical Functions, 9th print. Dover Publications, New York, 1046 pp.

Amos, C.L., Bowen, A.J., Huntley, D.A. and Lewis, C.F.M., 1988. Ripple generation under combined influence of waves and currents on the Canadian continental shelf. Cont. Shelf Res., 8: 1129–1153.

Brebner, A., 1980. Sand bed-form lengths under oscillatory motion. In: Proc. 17th Int. Conf. Coastal Eng., Sidney. ASCE, pp. 1340–1343.

Cacchione, D.A. and Drake, D.E., 1982. Measurements of storm generated bottom stresses on the continental shelf. J. Geophys. Res., 87: 1952–1961.

Cacchione, D.A., Grant, W.D., Drake, D.E. and Glenn, S.M., 1987. Storm-dominated bottom boundary layer dynamics on the northern California continental shelf: Measurements and predictions. J. Geophys. Res., 92: 1817–1827.

Drake, D.E. and Cacchione, D.A., 1986. Field observations of bed shear stress and sediment resuspension on shelves. Cont. Shelf Res., 6: 415–429.

Drake, D.E. and Cacchione, D.A., 1989. Estimates of the suspended sediment concentration ($C_{\rm a}$) and resuspension coefficient (γ_0) from near-bottom observations on the California shelf. Cont. Shelf Res., 9: 51–64.

Glenn, S.M. and Grant, W.D., 1987. A suspended sediment stratification correction for combined wave and current flows. J. Geophys. Res., 92: 8244–8264.

Graber, H.C. and Madsen, O.S., 1988. A finite-depth wind-wave model. Part I: Model description. J. Phys. Oceanogr., 18: 1465–1483.

Grant, W.D. and Madsen, O.S., 1982. Movable bed roughness in unsteady oscillatory flow. J. Geophys. Res., 87: 469–481.

Green, M.O., Rees, J.M. and Pearson, N.D., 1990. Evidence for the influence of wave-current interaction in a tidal boundary layer. J. Geophys. Res., 95: 9629–9644.

Gross, T.F., Isley, A.E. and Sherwood, C.R., 1992. Estimation of stress and bed roughness during storms on the northern California shelf. Cont. Shelf Res., 12: 389–413.

Hasselmann, S. and Hasselmann, K., 1985. Computations and parameterizations of the nonlinear energy transfer in a gravity-wave spectrum. Part II: Parameterizations of the nonlinear energy transfer for application in wave models. J. Phys. Oceanogr., 15: 1378–1391.

Janssen, P.A.E.M., 1989. Wave induced stress and the drag of air flow over sea waves. J. Phys. Oceanogr., 19: 745–754.

Janssen, P.A.E.M., 1991. Quasi-linear theory of wind-wave generation applied to wave forecasting. J. Phys. Oceanogr., 21: 1631–1642.

Madsen, O.S. and Grant, W.D., 1976. Quantitative description of sediment transport by waves. In: Proc. 15th Int. Conf. Coastal Eng., Honolulu, HI. ASCE, pp. 1093–1112.

Madsen, O.S. and Rosengaus, M.M., 1988. Spectral wave attenuation by bottom friction: experiments. In: Proc. 21st Int. Conf. Coastal Eng., Malaga. ASCE, pp. 849–857.

Madsen, O.S., Poon, Y.-K. and Graber, H.C., 1988. Spectral wave attenuation by bottom friction: theory. In: Proc. 21st Int. Conf. Coastal Eng., Malaga. ASCE, pp. 492–504.

Madsen, O.S., Mathiesen, P.P. and Rosengaus, M.M., 1990. Movable bed friction factors for spectral waves. In: Proc. 22st Int. Conf. Coastal Eng., Delft. ASCE, pp. 420–429.

Mastenbroek, C., Burgers, G. and Janssen, P.A.E.M., 1993. The dynamic coupling of a wave model and a storm surge model through the atmospheric boundary layer. J. Phys. Oceanogr., 23: 1856–1866.

Shemdin, O., Hasselmann, K., Hsiao, S.V. and Heterich, K., 1978. Nonlinear and linear bottom interaction effects in shallow water. In: Turbulent Fluxes through the Sea Surface, Wave Dynamics and Prediction. NATO Conf. Ser. V, Vol. 1, pp. 347–365.

SWIM Group, 1985. A shallow water intercomparison of three numerical wave prediction models (SWIM). Q. J. R. Meteor. Soc., 111: 1087–1112.

Tolman, H.L., 1991. A third-generation model for wind waves on slowly varying, unsteady and inhomogeneous depths and currents. J. Phys. Oceanogr., 21: 782–797.

Tolman, H.L., 1992. Effects of numerics on the physics in a third-generation wind-wave model. J. Phys. Oceanogr., 22: 1095–1111.

Tolman, H.L., 1994. Wind waves and moveable-bed bottom friction. J. Phys. Oceanogr., 24: 994–1009.

WAMDIG, 1988: The WAM model — a third generation ocean wave prediction model. J. Phys. Oceanogr., 18: 1775–1810.

Weber, S.L., 1991. Eddy-viscosity and drag-law models for random ocean wave dissipation. J. Fluid Mech., 232: 73–98.

Wilson, K.C., 1989. Friction on wave induced sheet flow. Coastal Eng., 13: 371–379.